Journal of Ovonic Research Vol. 13, No. 3, May - June 2017, p. 135 - 141

PREPARATION AND CHARACTERIZATION OF POROUS ZnO NANOSTRUCTURES GROWN ONTO SILICON SUBSTRATE

M. A. MAHDI[a*], A. RAMIZY[bc], H.F. AL-TAAY[d]
[a]*Basrah Nanomaterials Research Group (BNRG), Physics Department, College of Science, Basrah University, Basrah, Iraq.*
[b]*Department of Physics , College of Science, University of Anbar, Iraq*
[c]*Renewable energy Research Center, University of Anbar, Iraq*
[d]*Department of Physics, College of Science for Women, University of Baghdad, Baghdad,*

Zinc oxide (ZnO) thin film (approximately 1.1 μm) was synthesized onto a Si(100) substrate by radio frequency (rf) sputtering with 200 W rf power for 120 min. The porous nanostructure of the film was prepared through electrochemical etching with electrolyte solution containing ethanol and nitric acid at a current density of 50 mA/cm^2 and constant etching time of 120 s. Scanning electron microscopy images showed that the ZnO nanoparticles featured plate-like shape and covered the entire Si(100) substrate. After the porous process, the surface of the ZnO film became smooth, the plates or large particles disappeared, and nanosized pores were uniformly distributed. X-ray diffraction patterns confirmed that the ZnO/Si(100) thin film exhibited higher crystallinity, with hexagonal phase growing toward the c axis, than that of the porous ZnO/Si(100) nanostructure. The photoluminescence (PL) spectrum showed that the intensity of the near-band edge of the ZnO/Si peak was higher than that of the P–ZnO/Si peak. Furthermore, the number of defects in P–ZnO/Si(100) increased when the ratio of PL intensity for I_{UV} to I_{defect} decreased from 36.17 for ZnO/Si sample to 1.44 for porous ZnO/Si.

(Received March 30, 2017; Accepted June 2, 2017)

Keywords: ZnO nanostructure, Porous materials, Optical properties.

1. Introduction

Zinc oxide (ZnO) is one of the most important semiconductor oxides. ZnO exhibits interesting physical properties, such as wide band gap of ~3.37 eV at room temperature, large excitonic energy of ~60 meV, thermal stability, environment friendliness, chemical stability, low cost, and easy synthesis into nanostructured forms [1, 2]. ZnO nanostructures exhibit potential for various applications, such as solar cells [3], optical sensors [4], light-emitting diodes [5], and photocatalysts [6, 7]. ZnO is also used to fabricate gas sensor devices because of its good electrical conductivity responses to invisible gases, such as H_2, CO, alcohol, toluene, and methanol [8]. Nanocrystalline ZnO thin films can be prepared through physical methods, such as thermal evaporation [9], radio frequency (rf) magnetron sputtering [10], and molecular beam epitaxy [11]. The films can also be fabricated through chemical techniques, including hydrothermal method [12], sol–gel method [1], microwave-assisted chemical solution method, and chemical vapor deposition [13]. Porous materials contain pore voids and can be categorized based on the number of pores into low-, middle-, or high-porosity substances [14, 15]. The synthesis, characterization, and application of novel porous materials have gained increased attention for a wide range of applications, such as biomedical devices [16], solar cells [17], photo and gas sensors [18, 19], and photocatalysts [20]. Porous silicon can be used as substrates to prepare nanostructures, such as CdS nanoflowers [21] and ZnO nanocones [22]. Porous ZnO nanocrystalline structure can be onto porous silicon substrate. However, to our knowledge, preparing porous ZnO nanostructures by

*Corresponding author: mazinauny74@yahoo.com

electrochemical etching has not been reported yet. In the present work, porous ZnO nanostructure was grown through electrochemical etching. The morphology, crystalline structures, and optical properties of the prepared samples were investigated.

2. Experimental details and characterization tools

ZnO thin films were deposited onto an n-type silicon (Si) substrate at an orientation of (100). An Edwards Auto 500 RF sputtering system equipped with a QC Scientific Precision chiller was employed to sputter ZnO layers onto Si(100). Prior to the sputtering process, the native oxide layer on the substrate was removed using the Radio Corporation of America cleaning technique. The substrates were placed inside a sputter chamber, approximately 10 cm above the ZnO target. Two ZnO targets with 99.9% purity, dimension of 3.5 in, and ¼ thickness, were used to deposit the ZnO films. Deposition was initiated by vacuuming the sputter chamber at 5×10^{-5} mbar. Argon gas was introduced into the chamber until the pressure reached 2.3×10^{-2} mbar. Pre-sputtering process was performed for approximately 10 min. ZnO sputtering was conducted at a radio frequency (rf) power of 200 W for 120 min to allow the deposition of the ZnO layer onto the Si substrate. The sample was cut with a radius of 1 cm to match the size of the opened circular of the electrochemical cell and then placed in an electrolyte solution of (3:1) ethanol at 99.999%, HNO_3 at a concentration of 0.1%, current density of 50 mA/cm^2, and constant etching time of 120 s. Synthesis was conducted at room temperature. After etching, the samples were rinsed with ethanol and dried in nitrogen flow. The surface morphology of the prepared ZnO and porous ZnO/Si(100) nanocrystalline thin film was determined by scanning electron microscopy (SEM) (Leo-Supra 50VP, Carl Zeiss, Germany). Crystalline structure was determined using X-ray diffraction analysis (XRD) (X'Pert PRO MRD PW3040, PANalytical, the Netherlands) with Cu Kα (α = 0.154 nm) radiation. Photoluminescence (PL) and Raman shift spectra were investigated by HR 800 UV, HORIBA Jobin Yvon, Edison, NJ, USA at wavelengths of 325 and 514.5 nm, respectively.

3. Results and discussion

3.1. Surface morphology

Fig. 1a and 1b show the SEM micrographs of the as-prepared ZnO thin film and porous structure, respectively. The ZnO particles featured plate-like shape and covered the entire area of the Si substrate. However, the plates were corroded during the porous process, resulting in the disappearance of the ZnO belts. In addition, nanosized pores covered the Si substrate, and the surface of the ZnO thin films became smooth, thereby improving the surface morphology of the specimen. Distinct layers of pores with diameter ranging from 10 nm to 50 nm cover the entire surface area (Fig. 2). This result indicates gradual etching in the crystal center, leading to accurate etching of the grain boundaries. Conversely, the walls among the pores were thin with some short thin tips at the top. This condition indicates that the grain boundaries are etched slowly at the center of the crystals at high etching rates [23, 24].

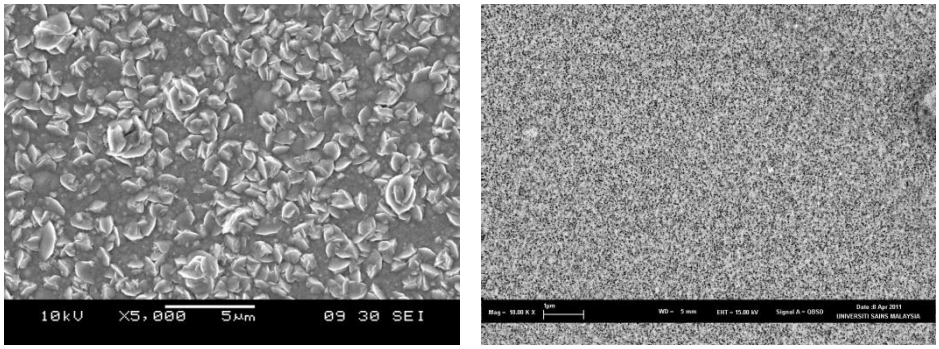

(a) (b)

Fig. 1. SEM images of (a) as-prepared Zn/Si(100) and (b) P–ZnO/Si(100) thin films

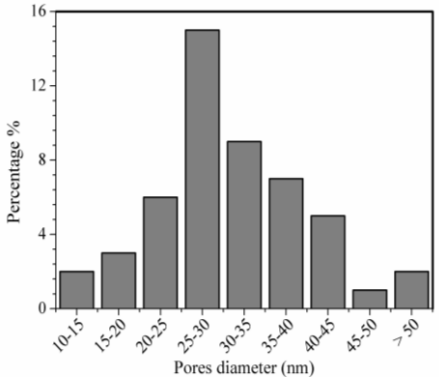

Fig. 2. Pore diameter distribution of P–ZnO/Si(100) thin film

3.2. Crystalline structure

Fig. 3 shows the XRD patterns of the as-prepared ZnO nanocrystalline thin film and porous sample. ZnO/Si sample showed high XRD intensity at a diffraction angle of 34.225°, and the porous ZnO/Si exhibited low diffraction intensity at an angle of 34.475°, which corresponds to the (002) plane of the ZnO structure. The diffraction angle of the (002) plane of the ZnO/Si thin films shifted toward lower angles compared with the standard XRD angle position of the ZnO thin film (34.42°) [25]. The angle of the (002) plane of the porous ZnO thin film is close to the standard position. The other diffraction peaks of the P–ZnO/Si thin film at 31.82° and 36.225° correspond to the (100) and (101) planes of ZnO wurtzite and ZnO crystalline structure, respectively. The absence of these planes from the XRD pattern of the as-deposited ZnO/Si thin films indicates the high orientation of the films along the c axis.

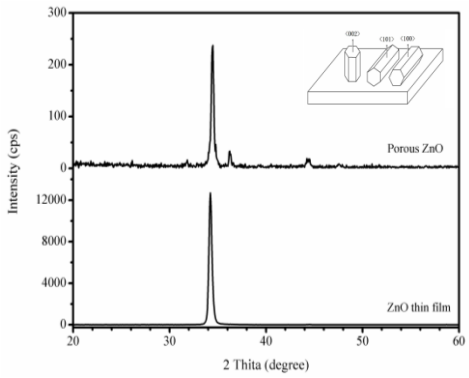

Fig. 3. XRD patterns of the as-prepared Zn/Si(100) and P–ZnO/Si(100) thin films.

The lattice parameters of hexagonal structures can be calculated using the formula [26]:

$$\frac{1}{d_{hkl}^{\ 2}} = \frac{4}{3}\left(\frac{h^2 + hk + l^2}{a^2}\right) + \frac{l^2}{c^2}, \tag{1}$$

where *a* and *c* are the lattice parameters. *h*, *k*, and *l* are the Miller indices.

The values of $\boldsymbol{c}$ were 5.2396 Å for the ZnO/Si thin film and 5.2074 Å for the porous ZnO/Si sample. The obtained value of $\boldsymbol{c}$ in the prepared and porous ZnO/Si samples is higher than the standard value in ZnO ($\boldsymbol{c_o}$ = 5.206 Å). This result indicates that the samples are affected by the presence of stress (σ), which can be calculated through the following relationship [1].

$$\sigma(GPa) = -233 \times \left[\left(c - c_o\right)/c_o\right] \times 100\% . \quad (2)$$

The stress value can be negative for compressive biaxial stress and positive for tensile biaxial stress. The calculated stress values in the plane perpendicular to the c axis of the ZnO/Si thin film and the P–ZnO/Si sample are −150.38% and −6.26%, respectively. Stress occurs because of two main reasons, namely, lattice mismatch between the thin film and substrate (extrinsic stress) or presence of impurities, defects, and lattice distortions in the thin film structure (intrinsic stress) [1]. The lattice mismatch for ZnO aligned with the c axis perpendicular to the Si surface reaches 40.16%, but the growth of the ZnO thin film at the c axis is parallel to the Si substrate surface, providing the epitaxial relationship ZnO(100)‖Si(100) lattice mismatch of ≈4% [27]. Thus, the higher compressive σ value of the ZnO/Si thin film than that of the P–ZnO/Si sample is related to intrinsic stress. Moreover, the porous process changed the concentration of impurities or defects inside the lattice of ZnO, resulting in decreased stress value (increasing ***c*** parameter value).

The strain along the c axis (ε) was estimated using the following equation:

$$\varepsilon = \left[\left(d_{film} - d_{powder}\right)/d_{powder}\right] \times 100\% , \quad (3)$$

where d_{film} is the d spacing of the ZnO thin film, and d_{powder} is the d spacing of ZnO powder. The ε values along the c axis of the ZnO/Si and P–ZnO/Si thin films are 0.645% and 0.0269%, respectively.

Ismail and Abdullah [10] prepared ZnO thin films onto Si(100) substrates by rf magnetron sputtering with different power intensities (150–250 W). The results indicated that all of the prepared samples exhibited a compressive stress, and the strain decreased from 0.749% to 0.618% as the power of synthesis increased from 150 W to 250 W [10].

3.3. Photoluminescence (PL) spectra

The room-temperature PL spectra of the as-grown ZnO nanocrystalline thin film and porous ZnO are shown in Fig. 4. The ZnO thin film showed higher ultraviolet (UV) intensity located at 382.37 nm, whereas the porous ZnO nanocrystalline thin film emitted a weak UV band peaked at 382.49 nm. The PL peaks of ZnO/Si and ZnO/Psi samples are close to optical band gap of pure ZnO [28]. However, this PL peak is attributed to the recombination in the near band edge of ZnO, confirming that the preparation of the ZnO thin films and porous structure showed good crystallization in agreement with the XRD analysis. Moreover, the violet peak intensity of ZnO/Si is higher than that of the P–ZnO/Si sample. This result is related to the high crystallinity of ZnO thin films prepared by rf sputtering. The PL broad band appearing in the visible region is related to the defective states in the ZnO lattice. Native or intrinsic defect of ZnO includes three types: missing atom at regular lattice position, extra atoms occupying interstices in the lattice, and zinc atom occupying oxygen site in lattice or vice versa [29]. Native defects in the lattice strongly influenced the electrical and optical properties of a semiconductor; these defects affected doping and minority carrier lifetime as well as luminescence activity. The native defects play an important role in ZnO conductivity because of the high level of unintentional n-type conductivity of ZnO, where O vacancies and Zn interstitials are regarded as sources of n-type conductivity in ZnO [29]. The defective PL bands of ZnO/Si are located at 509 and 760 nm, whereas those of the porous ZnO/Si sample are located at 577, 647, and 770 nm. The green emission peaks appearing at 509 nm for ZnO/Si and at 577 nm for porous ZnO/Si are related to zinc vacancy or to the singly ionized oxygen vacancy in ZnO, respectively; this emission is caused by the recombination of a photo-generated hole with the singly ionized charge state of the specific defect [30]. The yellow emission appearing in the PL spectrum of the prepared samples is attributed to oxygen vacancies and interstitial oxygen [31]. The ratio of PL intensity for I_{UV} to I_{defect} decreased from 36.17 for ZnO/Si sample to 1.44 for porous ZnO/Si, indicating the increase in the number of defects and surface trap states. This result indicates increased electron–hole recombination and emitted green or yellow light. The yellow emission is associated with both V_o and O_i; however, Marin et al. confirmed that this band is related to V_o when they annealed ZnO thin films prepared using sol–gel

method under various O_2 pressure levels [32]. Thus, the porous process of the ZnO nanocrystalline thin films could increase V_o in the crystalline structure, as evident by the high intensity of yellow emission. Marin et al. noted that the intensity of UV emission band is lower than V_o and V_{Zn} emissions for ZnO nanocones prepared onto porous silicon substrate by vapor transport at different temperatures and O_2 flow rates [22].

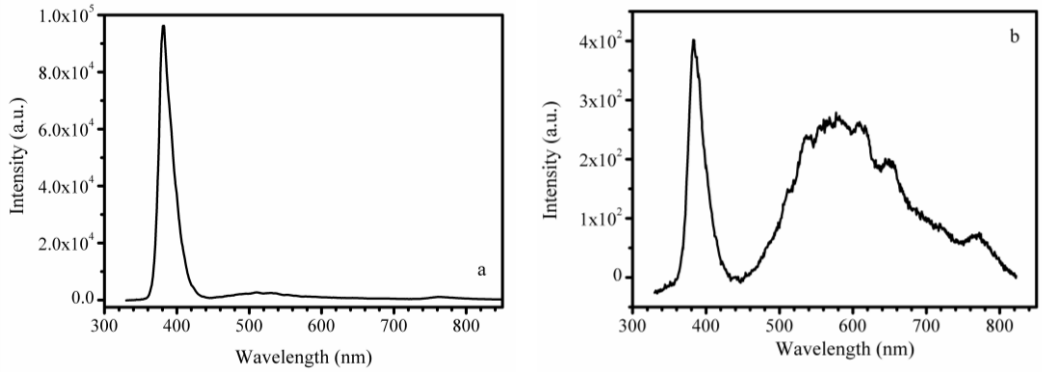

Fig. 4. PL spectra of (a) as-prepared Zn/Si(100) and (b) P–ZnO/Si(100) thin films.

3.4. Raman shift

Fig. 5 shows the Raman shift of the as-deposited ZnO/Si nanocrystalline thin film and porous ZnO/Si sample. The band at 376 cm^{-1} of ZnO/Si sample corresponds to Raman active zone-center optical phonons (A1) in transverse-optical (TO) mode [33]. However, the band at ~275 cm^{-1} is assigned to defect-induced modes of ZnO, as confirmed by recent theoretical studies [34]. The ZnO/Si and P–ZnO/Si samples show a weak Raman band located at a wavenumber of ~437 cm^{-1}, which is related to $E_2^{(2)}(high)$ of Raman active modes [33]. Yu et al. [35] prepared ZnO nanorods by hydrothermal method and observed Raman scattering peaked at 338 cm^{-1}, which is attributed to $E_2^{(2)}(high)$ mode of hexagonal wurtzite ZnO. The location of $E_2^{(2)}(high)$ in the ZnO nanostructures shifted because of many reasons, such as structure shape, preparation method, and impurity type and concentration [36, 37]. In addition, the ZnO/Si nanocrystalline thin films shows a band peaked at 579 cm^{-1}, which corresponds to A1(TO) mode. Furthermore, the Raman bands at ~520 and ~940 cm^{-1} correspond to the first-order transverse optical mode (1TO) and the second-order transverse optical phonon mode (2TO) of c-Si substrate, respectively [38].

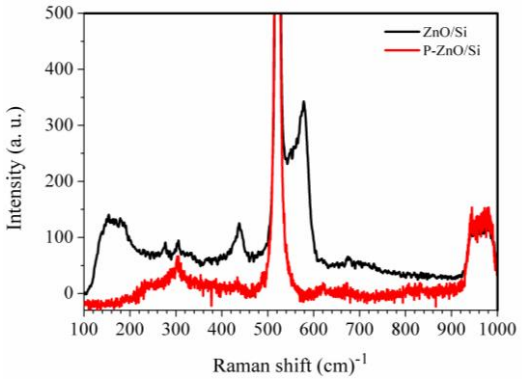

Fig. 5. Raman shift of the as-prepared Zn/Si(100) and P–ZnO/Si(100) thin films.

4. Conclusions

Porous ZnO nanocrystalline thin films were successfully prepared by electrochemical etching. The surface of ZnO thin films grown onto Si(100) substrate via rf sputtering contains different particle shapes and size. After the porous process, ZnO thin films showed smooth surface, with small pores covering the entire area of the ZnO film surface. XRD results confirmed that the crystallinity of ZnO thin films decreased after porous process, and the lattice parameter ***c*** became closer to the standard value than the as-prepared ZnO thin film. The calculated stress levels in plane perpendicular to the c axis of the ZnO/Si thin film and P–ZnO/Si sample are −150.38% and −6.26%, respectively. The impurities, defects, and lattice distortions in thin film structure led to intrinsic stress of the prepared samples. The PL spectra confirmed varied numbers of defects in the structure of the prepared samples, resulting in high values of stress between the ZnO/Si(100) and P–ZnO/Si(100) sample. In addition, the lower intensity of the violet PL peak of P–ZnO/Si(100) compared with that of the as-prepared ZnO thin film is related to the nanocrystalline nature of the sample after the porous process.

References

[1] M. B. Bouzour, A. E. Naciri, A. Moadhen, H. Rinnert, M. Guendouz, Y. Battie, A. Chaillou, M. A. Zaïbi, M. Oueslati, Mat Chem Phys **175**, 233 (2016).

[2] J. J. Hassan, M. A. Mahdi, Asmiet Ramizy, H. Abu Hassan, Z. Hassan, Superlattice Microst **53**, 31 (2013).

[3] Z. Li, G. Liu, Y. Zhang, Y. Zhoub, Y. Yang Mat Res Bull **80,** 191 (2016).

[4] J. J. Hassan, M. A. Mahdi, S. J. Kasim, Naser M Ahmed, H. Abu Hassan, Z. Hassan Appl Phys Lett **101**, 261108 (2012).

[5] J. J. Hassan, M. A. Mahdi, Y. Yusof, H. Abu-Hassan, Z. Hassan, H. A. Al-Attar, A. P. Monkman Opt Mater 3**5**, 1035 (2013).

[6] K. Maeda, K. Domen Chem Mate **22**, 612 (2010).

[7] Y. Wang, Y. Yang, L. Xi, X. Zhang, M. Jia, X. Xu, H. Wu Mate Lett **180**, 55 (2016)

[8] A. S. Kornyushchenko, A. H. Jayatissa, V. V. Natalich, V. I. Perekrestov, Thin Solid Films 604, 48 (2016).

[9] X. San, G. Wang, B. Liang, Y. Song, S. Gao, J. Zhang, F. Meng J Alloy Compd **622,** 73 (2015).

[10] A. Ismail, M. J. Abdullah, J King Saud University – Sci **25**, 209 (2013).

[11] B. Kim, G. Nam, Y. Park, H. Park, J. Y. Leem Korean J Met Mater **52**, 739 (2014).

[12] S. A. Azzeza, Z. Hassan, J. J. Hassan, R. Perumala, A. M. Selmane, M. Bououdina, Optik **127**, 9250 (2016).

[13] X. H. Wang, L. Q. Huang, L. J. Niu, R. B. Li, D. H. Fan, F. B. Zhang, Z. W. Chen, X. Wang, J Alloy Compd **622**, 440 (2015).

[14] Q. Xu, Nanoporous Materials: Synthesis and Applications, CRC Press, Taylor & Francis Group USA2013

[15] P. S. Liu, G. F. Chen, Porous Materials:Processing and Applications 1st edition Elsevier Inc., UK 2014

[16] G. Ryan, A. Pandit, D. P. Apatsidis Biomaterials **27**, 2651 (2006).

[17] W. A. Badawy J Adv Res **6**, 123 (2015).

[18] N. Naderi, M. R. Hashim, Int J Electrochem Sci **7,** 11512 (2012).

[19] Z Jing, J. Zhan Adv Mater **20**, 4547 (2008).

[20] J. Huang, H. Rena, X. Liua, X. Lia, J. J. Shimb Superlattice Microst **81**, 16 (2015).

[21] M. A. Mahdi, Asmiet Ramizy, Z. Hassan, S. S. Ng, J. J. Hassan, S. J. Kasim Chalcongenide Lett 9: 19. 2012

[22] O. Marin, G. Grinblat, A. M. Gennaro, M. Tirado, R. R. Koropecki, D. Comedi Superlattice Microst **79**, 29 (2015).

[23] J. A. Bardwell, I. G. Foulds, J. B. Webb, H. Tang, J. Fraser, S. Moisa, S. J. Rolfe J Electron. Mater **89,** 4142 (2001).

[24] Asmiet Ramizy, Saleh H. Abud, A. S. Hussein, Z. Hassan, F. K. Yam, C. W. Chin, Mat Sci Semicon Proc **29,** 102 (2015).
[25] S. Y. Ma, X. H. Yang, X. L. Huang, A. M. Sun, H. Song, H. B. Zhu, J Alloy Compd **566,** 9 (2013).
[26] B. B. He, Two-dimensional X-ray diffraction, John Wiley & Sons, Inc. , Hoboken, New Jersey, USA 2009.
[27] V. Khranovskyy, R. Yakimova Physica B: Condensed Matter **407**, 1533 (2012).
[28] Ü. Özgür, Y. A. Alivov, C. Liu, A. Teke, M. A. Reshchikov, J Appl Phys **98**, 041301 (2005)
[29] A. Janotti, C. G. Van de Walle, Rep Pro Phys **72,** 126501 (2009).
[30] S. Dogar, S. D. Kim Mat Sci Semicon Proc **56**: 127 (2016).
[31] M. Willander, O. Nur, J. R. Sadaf, M. I. Qadir, S. Zaman, A. Zainelabdin, N. Bano, I. Hussain Mater **3**, 2643 (2010).
[32] O. Marin, M. Tirado, N. Budini, E. Mosquera, C. Figueroa, D. Comed, Mat Sci Semicon Proc **56,** 2016 (2016)
[33] B. Hadzic, N. Romcevic, M. Romcevic, I. Kuryliszyn-Kudelska, W. Dobrowolski, U. Narkiewicz, D. Sibera Opt Mater **58**, 317 (2016)
[34] S. S. Kurbanov, H. C. Jeon, Z. S. Shaymardanov, R. Y. Rakhimov, T. W. Kang, J Luminesce **170**, 168 (2016).
[35] J. L. Yu, Y. F. Lai, S. Y. Cheng, Q. Zheng, Y. H. Chen J Luminesce **161**, 330 (2015).
[36] J. Kong, D. Fan, Y. Zhu Mat Sci Semicon Proc **15**, 258 (2012).
[37] D. Shuang, B. Wang, X. L. Zhong, H. L. Yan Mat Sci Semicon Proc **10,** 97 (2007).
[38] H. F. Al-Taay, M. A. Mahdi, D. Parlevliet, Z. Hassan, P. Jennings, Physica E **48,** 21 (2013).